Formation of Amorphous Alloys by Ion Beam Mixing and Its Multiscale Theoretical Modeling in the Equilibrium Immiscible Sc−W System

R. F. Zhang, Y. X. Shen, H. F. Yan, and B. X. Liu*

Advanced Materials Laboratory, Department of Materials Science and Engineering, Tsinghua University, Beijing 100084, China

Unique amorphous alloys are synthesized at the compositions of 25 and 40 atom % of W by ion beam mixing in the equilibrium immiscible Sc−W system characterized by a positive heat of formation of +14 kJ/mol. In thermodynamic modeling, a Gibbs free energy diagram is constructed based on Miedema's theory, and the diagram predicts a glass-forming range of the Sc−W system to be within 12−58 atom % of W. To develop an atomistic model, ab initio calculations are first conducted to assist the construction of an *n*-body Sc−W potential under the embedded atom method. The proven realistic potential is applied in molecular dynamic simulations to study the crystal-to-amorphous transition in the Sc−W solid solutions, thus determining the glass-forming ability of the system to be within 15−50 atom % of W. Apparently, both theoretical predicted glass-forming ranges cover the experimentally measured one, showing an excellent agreement. We report, in this paper, the experimental results from ion beam mixing and the multiscale theoretical modeling concerning the amorphous alloy formation in the Sc−W system together with a brief discussion of the structural transition mechanism.

1. Introduction

In synthesizing new materials of high performance for various applications, a great effort has been paid, in recent decades, to the development of nonequilibrium materials processing techniques which are capable of producing new metastable alloys or fabricating artificial solid-state microstructures.[1] For instance, ion beam mixing (IBM) of multiple metal layers was introduced in the early 1980s and has since been employed to study the metastable alloy formation in the binary metal systems.[2] Up to now, a number of amorphous alloys (or metallic glasses) and metastable crystalline alloys have been obtained by IBM in the binary metal systems,[3] frequently featuring negative heats of formation (ΔH_f), defined in Miedema's theory and calculated at an equiatomic stoichiometry.[4,5] Recently, IBM has advanced significantly in two respects. First, to increase the interfacial free energy stored in the multilayered samples, the individual layer thickness was intentionally designed to be a couple of nanometers, differing considerably from a typical thickness of 5−8 nm in the previously conducted IBM. Second, much interest has been switched to the systems characterized by positive ΔH_f, among which, some are essentially immiscible at equilibrium. Under such circumstances, the interfacial free energy was significantly increased and played an important role in elevating the initial multilayered films to an energetic level higher than those of the possible metastable states existing in the system of interest.[6] Based on the design of interfacial free energy, the authors' group has recently succeeded in producing amorphous alloys in the equilibrium immiscible Au−W and Ag−W systems.[7,8] In the present study, the Sc−W system with a large positive heat of formation (ΔH_f = +14 kJ/mol)[4] was selected to investigate the possibility of synthesizing nonequilibrium alloys by IBM as well as to reveal the detailed structural phase transition induced in the alternately deposited Sc−W

multilayered samples by ion irradiation. Second, thermodynamic calculation based on Miedema's theory is conducted to interpret the amorphous alloy formation in terms of comparing the relative energetic levels of the competing phases in question. Third, with the aid of ab initio calculations, an *n*-body potential of the Sc−W system is constructed and molecular dynamic (MD) simulations are then performed for determining the glass-formation ability/range (GFA/GFR) of the system. A brief discussion is followed to compare the calculated results with the experimental observations from IBM.

2. Experimental Procedure and Theoretical Methods

2.1. Experimental Procedure of Ion-beam Mixing. Four sets of Sc−W multilayered samples with overall compositions of $Sc_{75}W_{25}$, $Sc_{60}W_{40}$, $Sc_{40}W_{60}$, and $Sc_{25}W_{75}$, respectively, were designed and prepared by alternately depositing thin Sc and W layers at a rate of 0.5 Å/s onto NaCl single crystals as substrates in an evaporator with a base vacuum of 10^{-9} Torr. During deposition, no special cooling was provided to the substrates and the temperature rise of the substrates was estimated to be below 473 K. The total thicknesses of $Sc_{75}W_{25}$, $Sc_{60}W_{40}$, $Sc_{40}W_{60}$, and $Sc_{25}W_{75}$ multilayered samples were designed to be 42, 42, 40, and 40 nm, respectively, to match the projected range plus the projected range straggling of 200 keV xenon ions used in the present study. The desired compositions of the samples were obtained by adjusting the relative layer thicknesses of constituent metals and were later confirmed by energy-dispersive spectra (EDS) and Rutherford backscattering spectra (RBS) with an experimental error of 5%. Accordingly, the $Sc_{75}W_{25}$, $Sc_{60}W_{40}$, $Sc_{40}W_{60}$, and $Sc_{25}W_{75}$ multilayered samples consisted of 9, 13, 18, and 15 layers, respectively, in which the minimum thicknesses of the individual layers in the samples were about 2.0, 2.1, 2.2, and 2.0 nm, respectively. After deposition, the Sc−W multilayered films were analyzed by RBS and Figure 1 shows the corresponding RBS spectra, from which

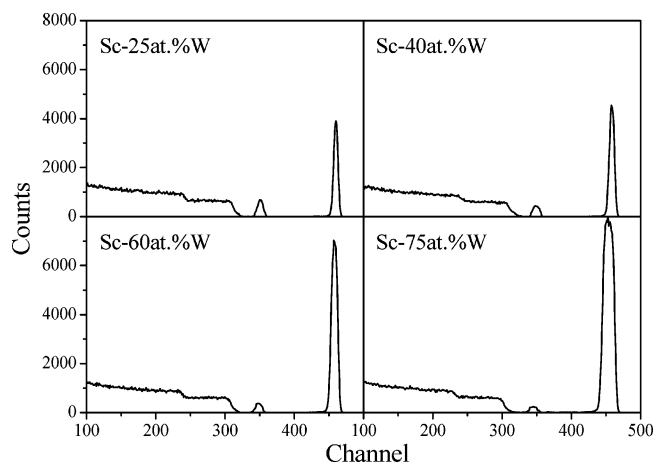* Corresponding author. E-mail: dmslbx@tsinghua.edu.cn.

4392 *J. Phys. Chem. B, Vol. 109, No. 10, 2005*

Zhang et al.

Figure 1. RBS spectra obtained for the as-deposited Sc−W multilayered samples.

the relative contents of Sc and W match approximately the designed overall compositions of the multilayered samples by SIMNI simulation.[9] The as-deposited multilayered samples were then irradiated by 200 keV xenon ions at room temperature in an implanter, which had a vacuum level on the order of 10^{-6} Torr, and the irradiation dose was in a range from 6×10^{14} to 9×10^{15} Xe$^+$/cm^2. The ion current density was controlled to be about $0.8-1$ μAcm^{-2} to minimize the beam heating effect. Under the above precautions, the effective temperature of the Sc−W multilayered samples during irradiation was measured to be around 353 K. For structural characterization, all the Sc−W multilayered samples were removed from the substrates by deionized water and put onto the Cu grids and then analyzed by transmission electron microscopy (TEM) and selected area diffraction (SAD). Incidentally, it will be discussed later that SAD analysis provides some indirect evidence in confirming the layered structures of the as-deposited Sc−W multilayered films.

2.2. Thermodynamic Calculation. Generally, the Gibbs free energy of an alloy phase can be calculated by $\Delta G = \Delta H - T \cdot \Delta S$, where ΔH and ΔS are the enthalpy and entropy terms, respectively. As a first approximation, the entropy term for a concentrated solid solution (CSS) and amorphous phase is simply taken as that of an ideal solution, i.e., $\Delta S = -R[c_A \ln c_A + c_B \ln c_B]$, where R is the gas constant and c_A and $\boldsymbol{c_B}$ are the atomic concentrations of metals A and B, respectively.

According to Miedema's theory and Alonso's method,[4,10−12] the enthalpy change ΔH is the sum of three terms, namely $\Delta H = \Delta H^c + \Delta H^e + \Delta H^s$, corresponding to the chemical, elastic, and structural contributions, respectively.

The chemical term ΔH^c is closely related to the electron redistribution generated at the boundary for the Wigner−Seitz unit cell when alloying, and can be calculated by,

$$\Delta H^c = c_A c_B [c_B \Delta \bar{H}_{AinB}^{inter} + c_A \Delta \bar{H}_{BinA}^{inter}] \qquad (1)$$

where $\Delta \bar{H}_{AinB}^{inter}$ and $\Delta \bar{H}_{BinA}^{inter}$ are the solution enthalpies of A solved in B and that of B solved in A, respectively, and all these values have been compiled by Niessen et al. [4,10]

In a similar way, the elastic term ΔH^e for a CSS is caused by the atomic size mismatch of the two constituent metals and can be expressed by taking the weighted average of the mismatch energies,[4,10]

$$\Delta H^e = c_A c_B [c_B \Delta \bar{H}_{AinB}^{elastic} + c_A \Delta \bar{H}_{BinA}^{elastic}] \qquad (2)$$

where $\Delta \bar{H}_{AinB}^{elastic}$ and $\Delta \bar{H}_{BinA}^{elastic}$ are the partial elastic mismatch energies for A solved in B and B solved in A, respectively, and all these values can be found in some published books and/or comprehensive papers.[4,10]

The structural term ΔH^s is deduced from the lattice stability $E(Z)$ of the bcc, fcc, and hcp structures as a function of the number of valence electrons Z of the metal,[4,10]

$$\Delta H^s = E(Z) - c_A E(Z_B) - c_B E(Z_A) \qquad (3)$$

where $E(Z)$, $E(Z_A)$, and $E(Z_B)$ are the lattice stability of the CSS and pure metals A and B, and Z, Z_A, and Z_B are the mean numbers of valence electrons of the CSS and the numbers of valence electrons of pure metals A and B, respectively. [4,10]

Comparing with the CSS, the structural and elastic terms for the formation enthalpy of an amorphous alloy are absent or significantly reduced, i.e., $\Delta H^e \approx 0$ and $\Delta H^s \approx 0$. There is, however, apart from the chemical term, another term contributing to the formation enthalpy of the amorphous alloy that reflects the relative disordering and therefore the formation enthalpy of the amorphous alloy can be expressed by, [4,10]

$$\Delta H^{amorphous} = \Delta H^c + \Delta H^{topological} \qquad (4)$$

where the topological enthalpy $\Delta H^{topological}$ accounts for the difference between the crystalline and amorphous states, which can be calculated by, [4,10]

$$\Delta H^{topological} = 3.5 \cdot (c_A T_{m,A} + c_B T_{m,B}) \qquad (5)$$

where $T_{m,A}$ and $T_{m,B}$ are the melting temperatures of the metals A and B, respectively. Meanwhile, the chemical term of the amorphous alloy ΔH^c can be assumed to be equal to that of the CSS.

The Gibbs free energy of the initial state of the A−B multilayered samples should be calculated by adding the interfacial free energy to the ground state (i.e., the zero line) representing a mechanical mixture of A and B in the bulk form. According to Zhang et al.,[4,13−15] the excess interfacial free energy of the multilayered samples can be calculated by $\Delta G_{mul} = \alpha_A S_{fA} \gamma_{BA}^{SS} + \alpha_B S_{fB} \gamma_{AB}^{SS}$, where S_{fA} and S_{fB} are the surface areas occupied by one mole of atoms A and B, respectively, the parameters α_A and α_B are the fraction of interfacial atoms A and B versus the total number of atoms in the multilayered samples, and γ_{AB}^{SS} (or γ_{BA}^{SS}) is the interfacial free energy of 1 mol of atoms A (or B) solved in B (or A). These terms can easily be calculated following the well-documented literatures.[4,13−15]

2.3. Method of ab Initio Calculations. The first-principles calculation is based on the well-established Vienna ab initio simulation package (VASP).[16] In the package, the calculations are conducted in a plane-wave basis, using fully nonlocal Vanderbilt-type ultra-soft pseudopotentials to describe the electron−ion interaction,[17] which allows the use of a moderate cutoff for the construction of the plane-wave basis for the transition metals (241.62 eV in the present calculations). In the calculation, the exchange and correlation items are described by the generalized-gradient approximation (GGA) proposed by Perdew and Wang.[18] The integration in the Brillouin zone is done on special k points ($11 \times 11 \times 11$ Monkhorst−Pack grid leading to 56 irreducible k points in the present study) determined according to the Monkhorst−Pack scheme.[19]

In the present study, the cohesive energies and the lattice constants of two simple ordered structures, i.e., the L1$_2$ structure

Formation of Amorphous Alloys

J. Phys. Chem. B, Vol. 109, No. 10, 2005 **4393**

for the compositions of $Sc_{75}W_{25}$ and the B2 structure for the composition of $Sc_{50}W_{50}$, are calculated and later employed in deriving the *n*-body potential.

2.4. Method for Construction of *n*-Body Potential. In the present study, an *n*-body Sc−W potential is constructed under the framework of a well-known embedded atom method (EAM).[20] In the EAM, the total energy E_{tot}, which can be written as a unique function of the electron density ρ_i, is mainly the energy to embed the atom into the electron density of the neighboring atoms, and supplemented by a short-range doubly screened pair interaction, which accounts for the core−core repulsions.[21] Consequently, the total energy can be expressed by,

$$E_{tot} = \sum_i F_i(\rho_i) + \frac{1}{2}\sum_{i,j(i \neq j)} \phi_{ij}(r_{ij}) \quad (6)$$

where $F(\rho_i)$ is the energy required to embed atom *i* into the background electron density ρ_i, and $\rho_i = \sum_{j \neq i} f_j(r_{ij})$. $f_j(r_{ij})$ is the electron density at the site of atom *i* contributed by atom *j*. $\phi_{ij}(r_{ij})$ and r_{ij} are respectively the short-range pair potential and the separated distance between atom *i* and atom *j*. The electron density function is commonly taken as an exponentially decreasing function,[22] and at a first approximation, the atomic electron density $f(r)$ takes a function form of $f(r) = f_e \exp[-\chi(r/r_e - 1)]$ for both hcp and bcc metals, where f_e is a scaling factor determined by the cohesive energy E_c and the atomic volume Ω. r_e is an equilibrium nearest distance, and χ is an adjustable parameter to be fitted. The embedding function adopts a universal form suggested by Banerjea[22] and Cai.[23] Accordingly, the embedding function can be expressed by,

$$F(\rho_i) = -F_0\left[1 - \ln\left(\frac{\rho_i}{\rho_e}\right)^n\right]\left(\frac{\rho_i}{\rho_e}\right)^n + F_1\left(\frac{\rho_i}{\rho_e}\right) \quad (7)$$

where $F_0 = E_c - E_v^f$ and E_v^f is the vacancy formation energy. F_1 is an adjustable parameter for the hcp metal and it is set to be zero for the bcc metal. ρ_e is the host electron density at an equilibrium state. According to Banerjea and Smith,[22] a decreasing exponential curvature function combining with the universal embedding function could yield the model function of Rose et al.[24] Consequently, the function proposed by Cai and Ye[23] for the fcc metals is adopted and modified a little for the pair potential $\phi(r)$ of the hcp metals in the present study,

$$\phi_{hcp}(r) = -\alpha[1 + \beta(\{r/r_e\} - 1)]\exp[-\beta(\{r/r_e\} - 1)] \quad (8)$$

Meanwhile, the function proposed by Johnson and Oh[25] is used for the pair potential of the bcc metals in the present study,

$$\phi_{bcc}(r) = \Phi(r) = k_0 + k_1(\{r/r_e\} - 1) + k_2(\{r/r_e\} - 1)^2 +$$
$$k_3(\{r/r_e\} - 1)^3, \quad r_e \leq r \leq r_s$$
$$= \Phi_a(r) = \Phi(r) + k_a[\Phi(r) - \Phi(r_e)](\{r/r_e\} - 1)^2,$$
$$r < r_e \quad (9)$$

where *r* is the interatomic distance, r_e is an equilibrium first-neighbor distance, k_a is a constant in the form of $k_a = 4.5(1 + 4/(A_r - 0.1))$ depending on an anisotropy ratio A_r, and the cutoff distance (from r_s to r_c) is set to be between the second- and third-neighbor distances.[26]

The hcp−bcc cross potential takes a simplified form, which was recently proposed for the fcc−bcc metal systems by Gong et al.,[27] to combine the hcp−hcp and bcc−bcc potentials,

$$\phi_{hcp-bcc}(r) = A[\phi_{hcp}(r + B) + \phi_{bcc}(r + C)] \quad (10)$$

where *A*, *B*, and *C* are three potential parameters to be fitted.

2.5. Scheme of Molecular Dynamic Simulations. Based on the constructed EAM potential for the Sc−W system, MD simulation is carried out with the Parrinello−Rahman constant pressure scheme and the equations of motion are solved through a fourth-order predictor−corrector algorithm of Gear with a time step of $t = 5 \times 10^{-15}$ s.[28] In the present study, two kinds of simulation models are employed for the Sc−W system, i.e., for the Sc-rich side, an hcp solid solution model consisting of $10 \times 10 \times 6 \times 2 = 1200$ atoms, and for the W-rich side, a bcc solid solution model containing $9 \times 9 \times 8 \times 2 = 1296$ atoms, respectively. In the simulation models, the (100), (010), and (001) atomic crystal directions are parallel to the *x*, *y*, and *z* axes, respectively, and the periodic boundary conditions are adopted in three dimensions. To obtain a specific chemical stoichiometry for the Sc−W alloy, a desired number of Sc (W) atoms in the original hcp (bcc) lattice are randomly substituted by W (Sc) atoms. In the present study, MD simulation is conducted at room temperature (300 K) for adequate MD time steps (2 ns) until all the dynamic parameters show no secular variation.

3. Results and Discussion

3.1. Experimental Results. We now present the experimental results from IBM. Parts a and b of Figure 2 show the typical selected area diffraction (SAD) patterns of the as-deposited state and the irradiated state at a dose of 3×10^{15} Xe$^+$/cm^2, respectively, for the $Sc_{75}W_{25}$ multilayered samples. From Figure 2a, one can clearly see the sharp diffraction rings, which can be indexed to be from a polycrystalline hcp-Sc and a bcc-W, suggesting that in the as-deposited state, Sc and W were not mixed and most likely located in the separated Sc and W layers. When the $Sc_{75}W_{25}$ multilayered samples were subjected to 200 keV xenon ion irradiation at room temperature to doses lower than 5×10^{15} Xe$^+$/cm^2, the crystalline Sc and W remain, except some diffraction lines from bcc-W gradually widen as shown in Figure 2b. When the $Sc_{75}W_{25}$ multilayered samples were subjected to a further irradiation dose of 7×10^{15} Xe$^+$/cm^2, the widened diffraction lines disappeared gradually and transformed into some diffused halos as shown in Figure 2c, indicating that an amorphous phase was gradually formed. Finally, a unique amorphous phase was obtained at an irradiation dose of 9×10^{15} Xe$^+$/cm^2 and the corresponding SAD pattern is shown in Figure 2d. Comparing parts d and a of Figure 2, one can observe that the diffraction lines reflected from crystalline Sc and W have disappeared completely, and only the diffused halos are shown, indicating the formation of a unique amorphous phase. For the $Sc_{60}W_{40}$ multilayered samples, similar structural transition was also observed, as can be observed from the SAD patterns exhibited in parts a and b of Figure 3 for its as-deposited state and irradiated state at a dose of 9×10^{15} Xe$^+$/cm^2, respectively. From Figure 3b, it can be seen clearly that the initial crystalline Sc and W have transformed into an unique amorphous phase at an irradiation dose of 9×10^{15} Xe$^+$/cm^2 and the detailed structural phase transition is somehow similar to that appearing in the $Sc_{75}W_{25}$ samples.

For the W-rich side, Figure 4a exhibits a SAD pattern to show the structure of the as-deposited state of the $Sc_{40}W_{60}$ sample.
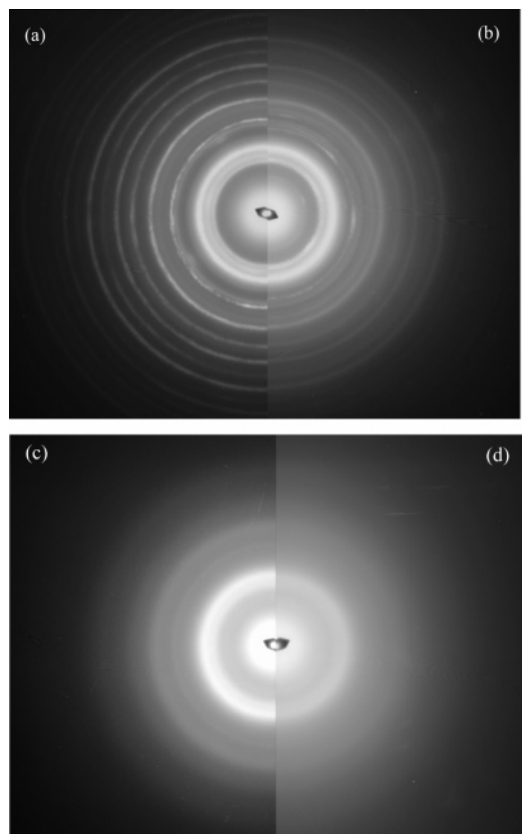
Figure 2. Selected area diffraction patterns for the $Sc_{75}W_{25}$ multilayered samples with 9 layers: (a) the as-deposited state, (b) the irradiated state at an irradiation dose of 3×10^{15} Xe$^+$/cm^2, (c) the irradiated state at an irradiation dose of 7×10^{15} Xe$^+$/cm^2, and (d) a unique amorphous phase formed at an irradiation dose of 9×10^{15} Xe$^+$/cm^2.

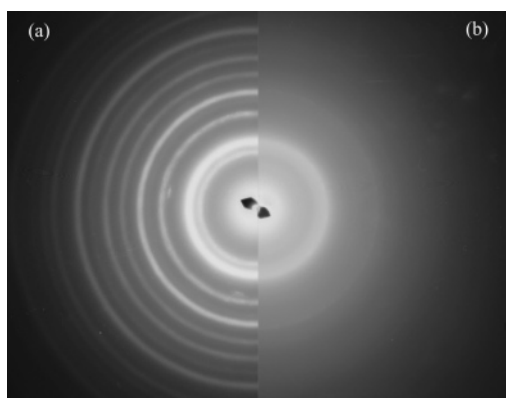**Figure 3.** Selected area diffraction patterns for the $Sc_{60}W_{40}$ multilayered samples with 13 layers: (a) the as-deposited state and (b) an amorphous phase formed at an irradiation dose of 9×10^{15} Xe$^+$/cm^2.

From the pattern, one can clearly see that the W diffraction rings are sharp, while the diffraction lines of Sc are very weak, indicating that Sc was not well crystallized. When the samples were subjected to irradiation by 200 keV xenon ions, a metastable crystalline (MC) phase of bcc structure (lattice constant $a = 3.39 \pm 0.05$ Å) was formed and remained unchanged up to an irradiation dose of 5×10^{15} Xe$^+$/cm^2. A typical SAD pattern of the MC bcc phase formed at an irradiation dose of 3×10^{15} Xe$^+$/cm^2 is exhibited in Figure 4b. These results mean that the MC bcc phase could be relatively stable upon irradiation as long as it was formed. Further increasing the irradiation dose from 5×10^{15} Xe$^+$/cm^2 to 9×10^{15} Xe$^+$/cm^2, a crystalline-to-amorphous transition occurred in the samples. Figure 4c exhibits a SAD pattern taken at an

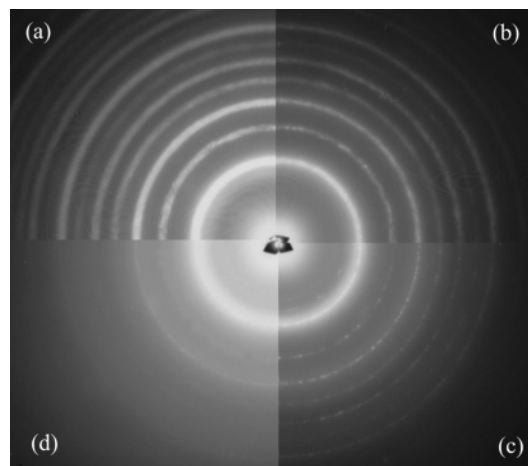**Figure 4.** Selected area diffraction patterns for the $Sc_{40}W_{60}$ multilayered samples with 18 layers: (a) the as-deposited state, (b) the irradiated state at an irradiation dose of 5×10^{15} Xe$^+$/cm^2, (c) the irradiated state at an irradiation dose of 7×10^{15} Xe$^+$/cm^2, and (d) the irradiated state at an irradiation dose of 9×10^{15} Xe$^+$/cm^2.

TABLE 1: Structural Phase Evolution in the Sc−W Multilayered Samples upon IBM to Various Ion Doses[a]

alloy system	$Sc_{75}W_{25}$	$Sc_{60}W_{40}$	$Sc_{40}W_{60}$	$Sc_{25}W_{75}$
as-deposited	Sc + W	Sc + W	bcc	bcc
6×10^{14} Xe$^+$/cm^2	Sc + W	Sc + W	bcc	bcc
8×10^{14} Xe$^+$/cm^2	Sc + W	Sc + W	bcc	bcc
1×10^{15} Xe$^+$/cm^2	Sc + W	Sc + W	bcc	bcc
3×10^{15} Xe$^+$/cm^2	Sc + W	Sc + W	bcc	bcc
5×10^{15} Xe$^+$/cm^2	Sc + W	Sc + W	bcc	bcc
7×10^{15} Xe$^+$/cm^2	PA	PA	bcc	bcc
9×10^{15} Xe$^+$/cm^2	A	A	Bcc + PA	bcc

[a] bcc, bcc solid solution; A, completely amorphized; PA, partially amorphized.

irradiation dose of 7×10^{15} Xe$^+$/cm^2. It can be seen that the MC bcc phase has partially transformed into an amorphous phase, and finally at an irradiation dose of 9×10^{15} Xe$^+$/cm^2, most of the bcc phase has transformed into the amorphous phase, as only a few very weak diffraction rings reflected from a trace amount of crystalline W can still be visible in the SAD pattern shown in Figure 4d. Through a detailed analysis by EDS, the composition of the amorphous phase seen in the SAD pattern is estimated to be about 48 atom % of W. As for another composition, i.e., the $Sc_{25}W_{75}$ multilayered samples, only the bcc phase ($a = 3.32 \pm 0.05$ Å) was found in the as-deposited state and it remained unchanged upon further irradiation from 6×10^{14} Xe$^+$/cm^2 to 9×10^{15} Xe$^+$/cm^2. Note that the lattice constants of the formed bcc phases in both $Sc_{40}W_{60}$ and $Sc_{25}W_{75}$ samples are a bit larger than that of the pure W ($a = 3.16$ Å), and the bcc phases can therefore be considered as a W-based bcc super-saturated solid solution (abbreviated as bcc-SSSS and hereafter).

To present the detailed structural phase transition in the four sets of Sc−W multilayered samples and furthermore to determine the GFR of the Sc−W system, the experimental results for the four sets of multilayered samples irradiated from 6×10^{14} Xe$^+$/cm^2 to 9×10^{15} Xe$^+$/cm^2 are listed in Table 1. From the table, one sees clearly that in the present study, the amorphous phase was obtained within the composition range of 25−48 atom % of W. Besides, the W-based bcc solid solution was formed within the composition range of 0−40 atom % of Sc.

3.2. Thermodynamic Calculation. Figure 5 is the Gibbs free-energy diagram of the Sc−W system constructed at room
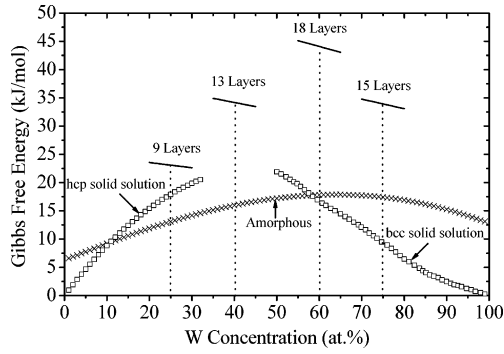
Formation of Amorphous Alloys

J. Phys. Chem. B, Vol. 109, No. 10, 2005 **4395**

Figure 5. Constructed Gibbs free energy diagram of the Sc−W system based on Miedema's theory and Alonso's method.

TABLE 2: Fitted Parameters for the Sc−Sc, W−W, and Sc−W Potentials

Sc−Sc		W−W		Sc−W	
χ	6.417256	c	6.155980	A	1.10885
α (eV)	0.311282	k_0 (eV)	−0.547671		
β	1.226141	k_1 (eV)	−2.130315	B (Å)	0.69826
r_a (Å)	2.662559	k_2 (eV)	16.808946		
F_1 (eV)	0.712605	k_3 (eV)	−8.503413	C (Å)	0.30702
r_s (Å)	3.4	r_s (Å)	3.2		
r_c (Å)	4.4	r_c (Å)	4.4		
n	1.25	n	0.44		

temperature based on Miedema's theory. From the diagram, it is found that the free energy of the initial multilayered samples is higher than that of the corresponding solid solutions and amorphous phases, and that the free energy of the amorphous phases is lower than that of the corresponding solid solutions within the composition range of 12−58 atom % of W, which can therefore be simply taken as the glass-formation range of the Sc−W system according to thermodynamic calculations.

3.3. Construction of *n*-body Sc−W Potentials. In the construction of *n*-body potentials for the pure hcp metals, the present authors propose the following fitting approach, i.e., using the average bulk and shear moduli, instead of five independent linear elastic constants, together with the cohesive energy, vacancy formation energy, and equilibrium lattice constants to fit the potential parameters, and after fitting, five independent linear elastic constants are reproduced by the fitted potentials, thus confirming the relevance of the fitting as well as the parameters. It turns out that the proposed fitting approach is fairly effective.

For the Sc−W system, fitting the potential parameters is also challenging work, because there is no equilibrium compound and no physical property could be used for fitting the cross potential. In this regard, there have been some reports[29,30] showing that the first-principles calculations could be of significant help in acquiring some useful physical properties of the alloy phases necessary for deriving *n*-body potentials. Accordingly, applying the Vienna ab initio simulation package, the total energies and the lattice constants of the possible nonequilibrium $Sc_{75}W_{25}$ and $Sc_{50}W_{50}$ compounds with $L1_2$ and B2 structures, respectively, are first calculated and then used in deriving *n*-body potentials of the Sc−W system. Concerning the details of the calculations and the fitting procedure, the readers can refer to our recent publication.[31] After the fitting and optimization, the potential parameters are obtained and Table 2 lists the fitted parameters for the Sc−Sc, W−W, and Sc−W potentials, respectively. Table 3 lists the comparison between some physical properties reproduced by the constructed potentials and from experimental/ab initio calculated values used initially for fitting the potentials.[32−34] Evidently, the constructed

TABLE 3: Comparison between the Calculated and Experimental Values of the Cohesive Energy E_c (eV), Lattice Constant a (Å) and c (Å), Average Bulk Moduli B (Mbar), Average Shear Moduli G (Mbar), and Vacancy Formation Energy E_v^f (eV) of Sc and W Metals at Room Temperature[32−34]

		E_c (eV)	a (Å)	c (Å)	B (Mbar)	G (Mbar)	E_v^f (eV)
Sc	exptl	3.90	3.308	5.267	0.558*	Sc−W*	1.15
	this work	3.90	3.308	5.267	0.558	0.3067	1.15
W	exptl	8.66	3.165		1.599*	3.1029*	3.95
	this work	8.66	3.165		1.599	3.1029	3.95
$Sc_{75}W_{25}$	ab initio	4.9244	4.34				
($L1_2$)	fitted	4.9471	4.28				
$Sc_{50}W_{50}$	ab initio	5.8245	3.31				
(B2)	fitted	5.9148	3.39				

potentials of the Sc−W system work reasonably well in terms of reproducing some physical properties of the pure Sc and W as well as those of the possible nonequilibrium $Sc_{75}W_{25}$ and $Sc_{50}W_{50}$ compounds. In addition, the energy differences between the three major crystalline structures for pure metals Sc and W are also calculated by the constructed potentials to be $E_{bcc} - E_{hcp} = 0.01$ eV and $E_{fcc} - E_{hcp} = 0.0001$ eV for Sc, while $E_{fcc/hcp} - E_{bcc} = 0.03$ eV for W, which are in good agreement with the well-known facts that hcp is the most stable structure for Sc and bcc for W, respectively, and could therefore serve as additional evidence confirming the relevance of the newly constructed potentials.

3.4. Molecular Dynamic Simulations. Employing the constructed Sc−W potential, MD simulations are carried out by using the hcp and bcc solid solution models, respectively. It has been shown that the GFR of a binary metal system is the composition range bounded by the two terminal critical solid solubilities, below which the solid solution would retain its crystalline state, while beyond which the solid solution would transform into a disordered/amorphous state.[3] Accordingly, in the hcp solid solution model, the amount of W solute atoms is gradually increased until reaching a critical value, at and beyond which the solid solution becomes energetically unstable and collapses into a disordered state, thus determining the critical solid solubility of W in Sc. Similar simulations are also performed to determine the critical solid solubility of Sc in W. As a typical example to show the determination of the critical solid solubility, Figure 6 exhibits the projections of atomic positions of the $Sc_{90}W_{10}$ and $Sc_{80}W_{20}$ solid solution models after annealing at 300 K for 2 ns, respectively. It can be seen vividly that a uniform disordered structure is formed in the $Sc_{80}W_{20}$ solid solution model, while the $Sc_{90}W_{10}$ solid solution model still remains in an ordered state, indicating that the critical solid solubility to trigger crystal-to-amorphous transition is between 10 and 20 atom % of W. We further study the composition from 10 to 20 atom % of W in detail, and find that the critical solid solubility of the Sc−W system is 15 atom % of W in Sc. Besides, it is commonly recognized that the total pair correlation functions are considered as a decisive measure to confirm a disordered state. Figure 7 exhibits the calculated total pair correlation functions of the Sc-based hcp and W-based bcc solid solution models, respectively, upon annealing at 300 K for 2 ns. In Figure 7, the left five lines are for the hcp solid solution models and the right five lines are for the bcc solid solution models. One sees clearly that in the Sc-rich side, beyond 20 atom % of W, the hcp solid solutions have transformed into the amorphous states, and that in the W-rich side, the bcc solid solutions remain in the crystalline states, suggesting that amorphous alloys can readily be formed in the Sc-rich side, whereas in the W-rich side, amorphous alloy can hardly be
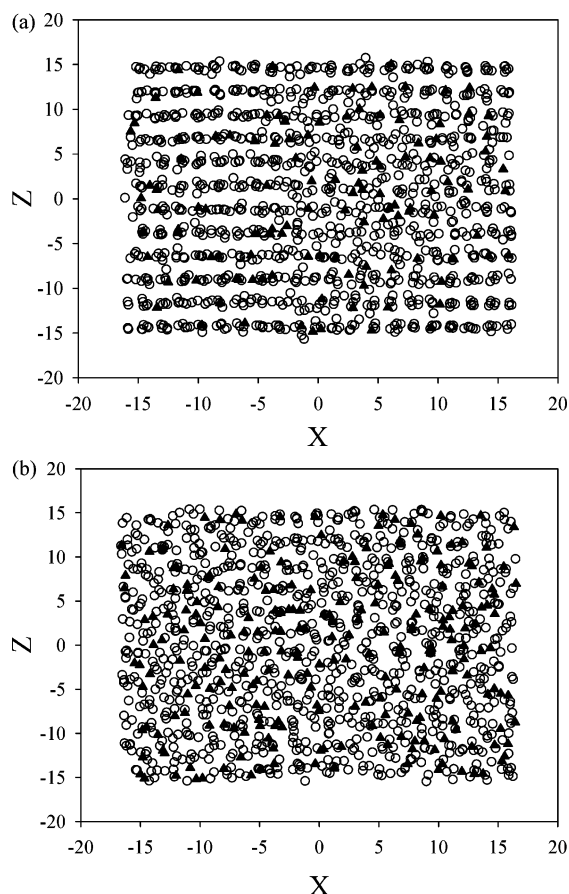
Figure 6. The projections of atomic positions of (a) $Sc_{90}W_{10}$ and (b) $Sc_{80}W_{20}$ solid solutions, respectively, after annealing at 300 K for 2 ns. Open circles: Sc. Filled triangles: W.
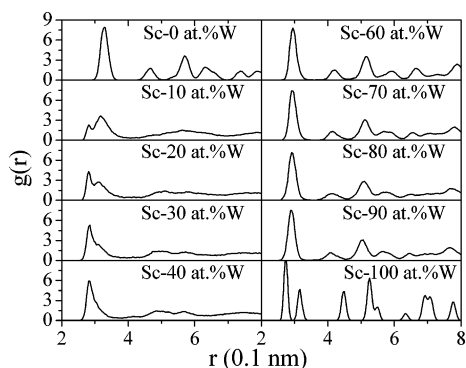

Figure 7. For the Sc−W system, the calculated total pair correlation functions of the solid solution models upon annealing at 300 K for 2 ns. (Note: the left five lines are for the hcp solid solution models and the right five lines are for the bcc solid solution models.)

obtained. Consequently, the GFR of the Sc−W system determined directly from the Sc−W potential through MD simulations is approximately within 15−50 atom % of W, which is in good agreement with the composition range of 25−48 atom % of W obtained from the present ion beam mixing experiments

3.5. Discussion. Comparing the calculated GFR by thermodynamic modeling described in section 3.2 and MD simulations described in section 3.4 with the experimentally determined GFR by ion beam mixing presented in section 3.1, one finds that the experimentally measured GFR of 25−48 atom % of W is a little narrower than the calculated GFR of 12−58 atom % of W and 15−50 atom % of W from thermodynamic calculation and molecular dynamic simulations, respectively, which is quite

reasonable, because, in general, two GFRs deduced from theoretical modeling predict the maximum possible GFRs. Moreover, the experimentally measured GFR at low W concentration limit is at 25 atom % of W, which is higher than the theoretical values, i.e., 12 and 15 atom % of W, obtained in the present study. This is because in ion beam mixing experiments, only the alloy compositions of 25 atom % of W and higher were studied and the alloy compositions lower than 25 atom % of W may need to be examined further. Besides, the experimentally measured GFR at high W concentration limit is 48 atom % of W, which is found to be quite close to that from MD simulations and quite compatible with that from thermodynamic calculations.

We now turn to discuss the possible mechanism responsible for the formation of the amorphous alloys in the $Sc_{75}W_{25}$ and $Sc_{60}W_{40}$ multilayered samples. As described by the thermodynamic calculations, the Gibbs free energy of the amorphous phase is lower than that of the corresponding initial multilayered samples as shown in Figure 5, meaning that the amorphous phase is energetically favored and is indeed obtained by IBM. Kinetically, the detailed process of IBM can generally be divided into two steps, i.e., a first step of atomic collision cascade triggered by the impinging ions followed by a second step of relaxation.[35] In the present study, the atomic collision cascade was responsible for inducing the interfacial diffusion of Sc atoms into its partner W lattices and vice versa, resulting in a highly energetic Sc−W mixture. During the second step of relaxation, the time period is extremely short, lasting only for $10^{-10}-10^{-9}$ s, and the effective cooling speed available can be as high as 10^{13-14} deg K/s,[36] which allows only an extremely limited rearrangement of the atoms in the Sc−W mixture resulting from the atomic collision taking place in the first step of IBM. Under such a high effective cooling speed, the Sc−W mixture is not allowed to relax straightforward to its corresponding equilibrium state, yet to reside at one of the possible intermediate states. In addition, the very short time of relaxation prevents the nucleation and growth process of an alloy phase with a complicated structure, as long-range diffusion is impossible. Consequently, only an amorphous or simple structured crystalline alloy phase can be formed in the highly energetic Sc−W mixture. In the present study, two Sc−W amorphous alloys are formed by IBM. From the point of view of atomic mobility, the present MD simulations also reveal the physical mechanism of amorphous alloy formation vividly, i.e., when the W solute atoms in the Sc lattice reached the values beyond the maximal solid solubility (i.e., 15 atom % of W), the crystalline Sc lattice collapsed and turned into a disordered state, resulting in formation of the amorphous alloy, as evidenced by a typical example shown in Figure 6.

In addition, in the W-rich side, another metastable bcc-SSSS was also obtained and the formation mechanism of bcc-SSSS is discussed as follows. Around the composition of $Sc_{40}W_{60}$, as described by the thermodynamic calculations shown in Figure 5, prior to forming an amorphous phase, a bcc-SSSS may first be obtained because the bcc-SSSS phase has a slightly higher energy than that of the amorphous phase. However, the energy difference between the amorphous phase and the bcc-SSSS is quite small. Consequently, as shown in Figure 4d, a small amount of crystalline bcc phase still remained and coexisted with an amorphous phase at an irradiation dose of 9×10^{15} Xe^+/cm^2. From a kinetic point of view, during the first step of the atomic collision cascade, a lower dose irradiation (lower than 7×10^{15} Xe^+/cm^2) was mainly responsible for the formation of the crystalline bcc-SSSS phase, while a higher dose

Formation of Amorphous Alloys

J. Phys. Chem. B, Vol. 109, No. 10, 2005 **4397**

irradiation (up to 9×10^{15} Xe$^+$/cm^2) was responsible for damaging the previously formed bcc-SSSS phase, thus leading to a disordered state. Consequently, the kinetically preferred formation sequence is that the bcc-SSSS phase was formed first and then the bcc-SSSS was damaged and transformed into an amorphous state. During the second step of relaxation, the extremely short time was responsible for transforming the bcc-SSSS into the amorphous phase. The above interpretation can clearly be confirmed from Figure 4, parts a–d. When the W concentration in the samples is more than 65 atom % of W, with the increase of W content, the free energy of the bcc-SSSS decreases more rapidly than that of the amorphous phase, and the energy difference increases considerably. As a result, the bcc phase may dominant while competing with the amorphous phase and with further increasing W concentration, e.g., in the Sc$_{25}$W$_{75}$ multilayered sample, only the bcc-SSSS has been obtained.

Now we give some further physical interpretation from the point of view of empirical diffusion dynamics concerning the metastable phase formation exhibited in the Sc–W system. Nordlund et al.[37] have studied the IBM process across the Co/Cu and Ni/Cu interface by simulations and found that the difference in melting points of the constituent metals could lead to different re-crystallization rates, and the diffusion coefficient of the metal with a low melting point is higher than that of the metal with a high melting point during the relaxation period. According to the model proposed by Chang et al.,[38] the amount of atomic transport due to radiation-enhanced diffusion was determined by the magnitude of atomic radius, radiation damage density, and cohesive energy. Among these parameters, cohesive energy plays a dominant role in atomic transport, and atoms with small cohesive energy are more mobile than those with large cohesive energy. For the Sc–W binary system, the melting temperature of Sc (1814 K) is much lower than that of W (3695 K) and the cohesive energy of Sc (3.9 eV/atom) is much lower than that of W (8.66 eV/atom).[32] It is therefore deduced that the Sc atoms might be more mobile during IBM, and they could diffuse into the W layers more easily than the W atoms migrating into the Sc layers. Based on the above discussion, the multilayered samples with lower Sc content, W-based bcc solid solution is more likely to be formed than the amorphous phase, which is consistent with our experimental observations in the Sc$_{40}$W$_{60}$ and Sc$_{25}$W$_{75}$ multilayered samples upon IBM.

4. Concluding Remarks

(1) Based on properly designing and controlling the interfacial free energy in the Sc–W multilayered films, a unique amorphous phase and a metastable W-based bcc solid solution are formed in the Sc-rich side and W-rich side, respectively, by ion beam mixing in the equilibrium immiscible Sc–W system.

(2) Thermodynamic modeling, based on Miedema's theory, predicts the possibility of synthesizing amorphous alloys in the Sc–W system within a composition range of 12–58 atom % of W, which is in good agreement with the experimentally measured GFR.

(3) Atomistic modeling based on an ab initio derived Sc–W potential predicts the glass-forming range of the Sc–W system to be within a composition range of 15–50 atom % of W, which matches fairly well with the experimentally measured GFR.

References and Notes

(1) Lu, Y. Q.; Zhu, Y. Y.; Chen, Y. F.; Zhu, S. N.; Ming, N. B.; Feng, Y. J. *Science* **1999**, *284*, 1822.

(2) Liu, B. X.; Johnson, W. L.; Nicolet, M. A.; Lau, S. S. *Appl. Phys. Lett.* **1983**, *42*, 45.

(3) Liu, B. X.; Lai, W. S.; Zhang, Q. *Mater. Sci., Eng. R* **2000**, *29*, 1.

(4) de Boer, F. R.; Boom, R.; Mattens, W. C. M.; Miedema, A. R.; Niessen, A. K. *Cohesion in Metals*: *Transition Metal Alloy*; North-Holland: Amsterdam, The Netherlands, 1989.

(5) Zhang, R. F.; Liu, B. X. *Appl. Phys. Lett.* **2002**, *81*, 1219.

(6) Li, Z. C.; Yu, D. P.; Liu, B. X. *Phys. Rev. B* **2002**, *65*, 245403.

(7) Zhang, R. F.; Liu, B. X. *J. Alloys Compd.* **2002**, *375*, 179.

(8) Zhang, R. F.; Liu, B. X. *J. Mater. Res.* **2003**, *18*, 1499.

(9) Ono, H.; Katsumata, T. *Appl. Phys. Lett.* **2001**, *78*, 1832.

(10) Bakker, H. *Enthalpies in Alloys*: *Miedema's Semi-Empirical Model*; Trans Tech: Zurich, Switzerland, 1998.

(11) Lopez, J. M.; Alonso, J. A. *Z. Naturforsch.* **1985**, *40a*, 1199.

(12) Alonso, J. A.; Gallego, L. J.; Simozar, J. A. *Nuovo Cimento* **1990**, *12*, 587.

(13) Miedema, A. R.; den Broeder, F. J. A. *Z. Metallkd.* **1979**, *70*, 14.

(14) Gerkema, J.; Miedema, A. R. *Surf. Sci.* **1983**, *124*, 351.

(15) Zhang, Z. J.; Liu, B. X. *Phys. Rev. B* **1995**, *51*, 8076.

(16) Kresse, G.; Hafner, J. *Phys. Rev. B* **1993**, *47*, 558.

(17) Vanderbilt, D. *Phys. Rev. B* **1990**, *41*, 7892.

(18) Perdew, J. P.; Wang, Y. *Phys Rev B* **1992**, *45*, 13244.

(19) Monkhorst, H. J.; Pack, J. D. *Phys. Rev. B* **1976**, *13*, 5188.

(20) Daw, M. S.; Baskes, M. I. *Phys. Rev. Lett.* **1983**, *50*, 1285.

(21) Foiles, S. M. *Phys. Rev. B* **1985**, *32*, 3409.

(22) Banerjea, A.; Smith, J. R. *Phys. Rev. B* **1988**, *37*, 6632.

(23) Cai, J.; Ye, Y. Y. *Phys. Rev. B* **1996**, *54*, 8398.

(24) Rose, J. H.; Smith, J. R.; Guinea, F.; Ferrante, J. *Phys. Rev. B* **1984**, *29*, 2963.

(25) Johnson, R. A.; Oh, D. J. *J. Mater. Res.* **1989**, *4,* 1195.

(26) Guellil, A. M.; Adams, J. B. *J. Mater. Res.* **1992**, *7*, 639.

(27) Gong, H. R.; Kong, L. T.; Lai, W. S.; Liu, B. X. *Phys. Rev. B* **2002**, *66*, 104204.

(28) Parrinello, M.; Rahman, A. *J. Appl. Phys.* **1981**, *52*, 7182.

(29) Luzzi, D. E.; Yan, M.; Sob, M.; Vitek, V. *Phys. Rev. Lett.* **1991**, *67*, 1894.

(30) Yan, M.; Sob, M.; Luzzi, D. E.; Vitek, V.; Ackland, G. J.; Methfessel, M.; Rodriguez, C. O. *Phys. Rev. B* **1993**, *47*, 5571.

(31) Zhang, R. F.; Kong, L. T.; Gong, H. R.; Liu, B. X. *J. Phys.*: *Condens. Matter* **2004**, *16*, 5251.

(32) Kittel, C. *Introduction to solid-state physics*, 6th ed.; Wiley: New York, 1986.

(33) Brandes, E. A.; Brook, G. B. *Smithells Metals Reference Book*, 7th ed.; Butterworth-Heinemann: Oxford, UK, 1992.

(34) Simmons, G.; Wang, H. *Single-Crystal Elastic Constants and Calculated Aggregate Properties: A Handbook*, 2nd ed.; MIT: Cambridge, MA, 1971.

(35) Liu, B. X.; Lai, W. S.; Zhang, Z. J. *Adv. Phys.* **2001**, *50*, 367.

(36) Thompson, M. W. *Defects and Radiation Damage in Metals*; Cambridge University Press: Cambridge, England, 1969.

(37) Nordlund, K.; Averback, R. S. *Phys. Rev. B* **1999**, *59*, 20.

(38) Chang, G. S.; Jung, S. M.; Song, J. H.; Kim, H. B.; Woo, J. J.; Byun, D. H. *Nucl. Instrum. Methods B* **1997**, *121*, 244.